Talanta 175 (2017) 297–304

Contents lists available at ScienceDirect

Talanta

journal homepage: www.elsevier.com/locate/talanta

Gold coated porous silicon nanocomposite as a substrate for photoluminescence-based immunosensor suitable for the determination of Aflatoxin B1

Valerii Myndrul[a], Roman Viter[b,*], Maryna Savchuk[c], Maryna Koval[a], Nikolay Starodub[c], Viesturs Silamiķelis[b], Valentyn Smyntyna[a], Arunas Ramanavicius[d,*], Igor Iatsunskyi[e,*]

[a] Experimental physics department, Odessa National I.I. Mechnikov University, 42, Pastera, 65026 Odessa, Ukraine
[b] Institute of Chemical Physics, and Institute of Atomic Physics and Spectroscopy, University of Latvia, 19 Raina Boulevard, LV 1586 Riga, Latvia
[c] National University of Life and Environmental Sciences, 15, Geroyiv Oborony, Kyiv 03041, Ukraine
[d] State Research Institute Center for Physical Sciences and Technology, Savanoriu ave. 231, LT-01108 Vilnius, Lithuania
[e] NanoBioMedical Centre, Adam Mickiewicz University, 85 Umultowska str., 61-614 Poznan, Poland

ARTICLE INFO

Keywords:
Porous silicon
Gold
Photoluminescence
Biosensor
Aflatoxin

ABSTRACT

A rapid and low cost photoluminescence (PL) immunosensor for the determination of low concentrations of Aflatoxin B1 (AFB1) has been developed. This immunosensor was based on porous silicon (PSi) covered by thin gold layer (Au) and modified by antibodies against AFB1 (anti-AFB1). PSi layer was formed on silicon substrate, then the surface of PSi was covered by 30 nm layer of gold (PSi/Au) using electrochemical and chemical deposition methods and in such ways PSi/$Au_{(El.)}$ and PSi/$Au_{(Chem.)}$ structures were formed, respectively. In order to find PSi/Au the most efficiently suitable for PL-based sensor design, structure several different PSi/$Au_{(El.)}$ and PSi/$Au_{(Chem.)}$ structures were designed while using different conditions for electrochemical or chemical deposition of gold layer. It was shown that during the formation of PSi/Au structure crystalline Au nanoparticles uniformly coated the surface of the PSi pores. PL spectroscopy of PSi/Au nanocomposites was performed at room temperature and it showed a wide emission band centered at 700 nm. Protein A was covalently immobilized on the surface of PSi/$Au_{(El.)}$ and PSi/$Au_{(Chem.)}$ forming PSi/$Au_{(El.)}$/Protein-A and PSi/$Au_{(Chem.)}$/Protein-A structures, respectively. In the next step PSi/$Au_{(El.)}$/Protein-A and PSi/$Au_{(Chem.)}$/Protein-A structures were modified by anti-AFB1 and in such way a structures (PSi/$Au_{(El.)}$/Protein-A/anti-AFB1 and PSi/$Au_{(Chem.)}$/Protein-A/anti-AFB1) sensitive towards AFB1 were designed. The PSi/$Au_{(El.)}$/Protein-A/anti-AFB1- and PSi/$Au_{(Chem.)}$/Protein-A/anti-AFB1-based immunosensors were tested in a wide range of AFB1 concentrations from 0.001 upon 100 ng/ml. Interaction of AFB1 with PSi/$Au_{(El.)}$/Protein-A/anti-AFB1- and PSi/$Au_{(Chem.)}$/Protein-A/anti-AFB1-based structures resulted PL quenching. The highest sensitivity towards AFB1 was determined for PSi/$Au_{(El.)}$/Protein-A/anti-AFB1-based immunosensor and it was in the range of 0.01–10 ng/ml. The applicability of PSi/Au-based structures as new substrates suitable for PL-based immunosensors is discussed.

1. Introduction

Contamination of food by mycotoxins is one of the most actual problems because the toxins are harmful to human and animal health. Aflatoxins (AF), which belongs to a group of mycotoxins, are often contaminating some food products such as cassava, corn, cotton seed, millet, peanuts, rice, sorghum, sunflower seeds, tree nuts, etc [1]. Aflatoxin B1 (AFB1) is one of the most dangerous forms of aflatoxins with significant toxic effects (e.g. teratogenicity, and carcinogenicity) [2], and it has residual risk in the initiation of human cancer (hepatocellular carcinoma (HCC)) [3]. Traditional methods for the determination of AFB1 are based on chromatography [4–6], and ELISA-Kits [7]. These methods are highly precise but long lasting and expensive. Therefore, less sophisticated and cheaper methods for the determination of toxin concentrations are required.

Some biosensors have been developed for the determination of AFB1. For instance, nanomolar concentrations of AFB1 have been precisely detected by electrochemical [8], field effect transistors (FET) [9], and optical transducers based biosensors [10,11]. Among a number of biosensors, the optical ones have some advantages such as

* Corresponding authors.
E-mail addresses: roman.viter@lu.lv (R. Viter), arunas.ramanavicius@chf.vu.lt (A. Ramanavicius), yatsunkiy@gmail.com (I. Iatsunskyi).

http://dx.doi.org/10.1016/j.talanta.2017.07.054
Received 30 May 2017; Received in revised form 15 July 2017; Accepted 19 July 2017
Available online 20 July 2017
0039-9140/

portability, low dimensions and high sensitivity towards selected analytes [12,13]. Sensitivity of optical biosensors can be improved by increased both optical signal detection area and signal-to-noise ratio. Therefore, the development of novel nanomaterials with high surface area and well established optical signal (e.g. absorption, reflectance, photoluminescence, etc.) might improve the performance of optical biosensors. Among optical biosensing techniques, the most advanced are fluorescence, surface enhanced Raman spectroscopy (SERS) and surface plasmon resonance (SPR). However these techniques are quite expensive and time consuming. In addition to mentioned techniques, photoluminescence can be also used as analytical signal in optical biosensors. Photoluminescence-based biosensors have higher sensitivity, they also are portable and less expensive than the other types of optical biosensors and traditional techniques, which are used for the determination of AFB1.

Among many different nanomaterials, porous silicon (PSi) is known as one of the most efficient material for the design of optical biosensors [14–17]. PSi is biocompatible, it has high surface to volume ratio, high reactivity of the surface, and good integration ability with a standard silicon semiconductor technology. PSi structural properties can be easily tuned according technical requirements and well adopted in design of optical biosensors. The main challenge for PSi-based biosensors is to prevent a degradation of surface due to oxidation in oxygen containing environment (e.g. air) and contamination by impurities [18]. The deposition of noble metal layers over PSi and formation of PSi/(noble metal) structure can partially prevent PSi from oxidation and contamination [18–20].

Recently, a number of papers have been published focusing on the applications of PSi/Au nanostructures in biomedicine [21,22], photovoltaics [23,24], biosensors [25–27], and Li-ion batteries [28]. It was shown, that surface plasmon resonance effects of layered PSi/Au structure are much higher comparing to that of unmodified PSi [29–31]. In addition PSi/Au structures demonstrated improved electrical, optical and sensing properties. It was reported that PSi/Au structures showed high rate of transfer of photogenerated charge carriers in Si/Au interface, which was used for the enhancement of biosensor sensitivity [27]. Due to well-developed methodology of covalent binding of biomolecules on the Au surface, PSi/Au structures are even more attractive for the design of biosensors. Au nanoparticles and/or Au-based nanolayers can be deposited onto the Si surface by various methods: electrochemical deposition [24], chemical reduction based synthesis [21], deposition of gold nanoparticles from colloidal solution [32] etc.

In this work, we report the structural and optical properties of electrochemically and chemically formed PSi/$Au_{(El.)}$ and PSi/$Au_{(Chem.)}$ structures. In order to design structures selective to AFB1 the surfaces of the PSi/$Au_{(El.)}$ and PSi/$Au_{(Chem.)}$ were functionalized by protein A (Protein-A), which was modified with antibodies against AFB1 (anti-AFB1) in the next step. Then both types of PSi/$Au_{(El.)}$/Protein-A/anti-AFB1 and PSi/$Au_{(Chem.)}$/Protein-A/anti-AFB1 structures were used in the design of photoluminescence (PL) based immunosensors suitable for the determination of AFB1 concentration. Sensitivity range and limit of detection (LOD) of both PSi/$Au_{(El.)}$/Protein-A/anti-AFB1 and PSi/$Au_{(Chem.)}$/Protein-A/anti-AFB1 structures towards AFB1 were calculated.

2. Results and discussion

2.1. Structural properties of PSi and PSi/Au

PSi and PSi/Au structures were investigated by XRD and SEM technique. Fig. 1 represents the XRD patterns of PSi, PSi/$Au_{(Chem.)}$ and PSi/$Au_{(El.)}$ structures. Within a measured range of 2θ, a distinct peak at 2θ = 28,35° corresponding to Si(111) structure is present in all patterns. In spectra of both (PSi/$Au_{(Chem.}^{0.5}$) and PSi/$Au_{(Chem.}^{20}$) structures no peaks that are characteristic for gold-based crystals were

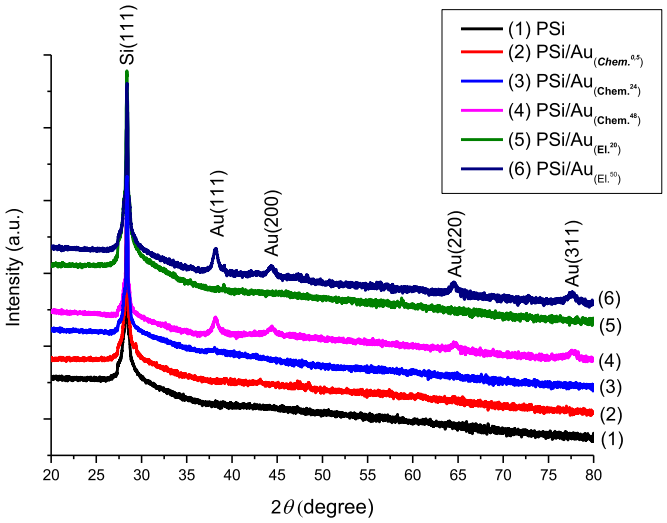

Fig. 1. The XRD patterns of PSi and PSi/Au structures.

observed, due to amorphous nature of deposited Au layer. Differently from previous two structures in spectra of both (PSi/$Au_{(El.}^{50}$) and PSi/$Au_{(Chem.}^{48}$)) structures four XRD peaks (at: 2θ= 38,18°, 2θ= 44,36°, 2θ = 64,62°, 2θ = 77,65°) were registered, these peaks are attributed to Au (111), Au (200), Au (220) and Au (311), respectively [31]. The fact that no peaks attributed to Au crystalline structures were observed in XRD spectrum of the PSi/$Au_{(El.}^{20}$) sample leads to conclusion that the potential of 20 mV *vs* Ag/$AgCl_{(3\ KCl)}$ is not high enough to form Au layer with well-defined crystalline structures.

In PSi/$Au_{(El.}^{50}$) and PSi/$Au_{(Chem.}^{48}$) structures a mean size of Au nanocrystallites was determined from XRD data using Scherer's equation [33]:

$$D = \frac{0.94\lambda}{FWHM \cdot \cos(\theta)}, \quad (1)$$

where D is the average size of nanocrystallites, λ – the peak maximum of X-ray wavelength, $FWHM$ – the width at half maximum of the XRD peaks registered at θ degree.

Calculated average size values of Au nanocrystallites in the PSi/$Au_{(Chem.}^{48}$) and PSi/$Au_{(El.}^{50}$) structures were equal to 13.0 ± 2 nm and 13.7 ± 4 nm, respectively. The average size of Au nanocrystallites was almost the same in both fabricated structures.

Fig. 2 represents the 'top-view' SEM images of the PSi/$Au_{(Chem.)}$ and PSi/$Au_{(El.)}$ structures. Pores of 2 μm diameter are uniformly distributed on the PSi surface is observed (Fig. 2a and b). The 'cross-sectional' SEM view showed that the average thickness of the PSi layer was about 130 μm (Fig. S1). Inner mesoporous structure of pores with average pore diameter of 13–30 nm was revealed by high resolution SEM based visualization (Fig. S1). Such mesoporous structure was formed due to competitive vertical and sidewall isotropic etching of the bulk Si substrate [19,34].

SEM images of PSi/$Au_{(Chem.)}$ structures are presented in Fig. 2c and d, which both reveals that the PSi substrates were well covered by gold layer that consisted of Au-based agglomerates of large surface with average size of 150 nm were uniformly distributed on the PSi surface (Fig. 2c and d). The SEM data are in good agreement with XRD data. In order to get crystalline Au-based structures on PSi longer duration of chemical deposition is required.

The formation of seed layer is a key factor of gold electrodeposition on PSi surface [35]. Gold nanoparticle formation using $HAuCl_4$, as an oxidation agent, and tannin as an reducing agent for chemical deposition process can be described by such chemical reaction [31]:

$$[AuCl_4]^-(aq.) + 3e^- \xrightarrow{Tannin} Au^0 + Cl^-. \quad (2)$$

Complex ion of $[AuCl_4]^-$ due to interaction with tannin is reduced to

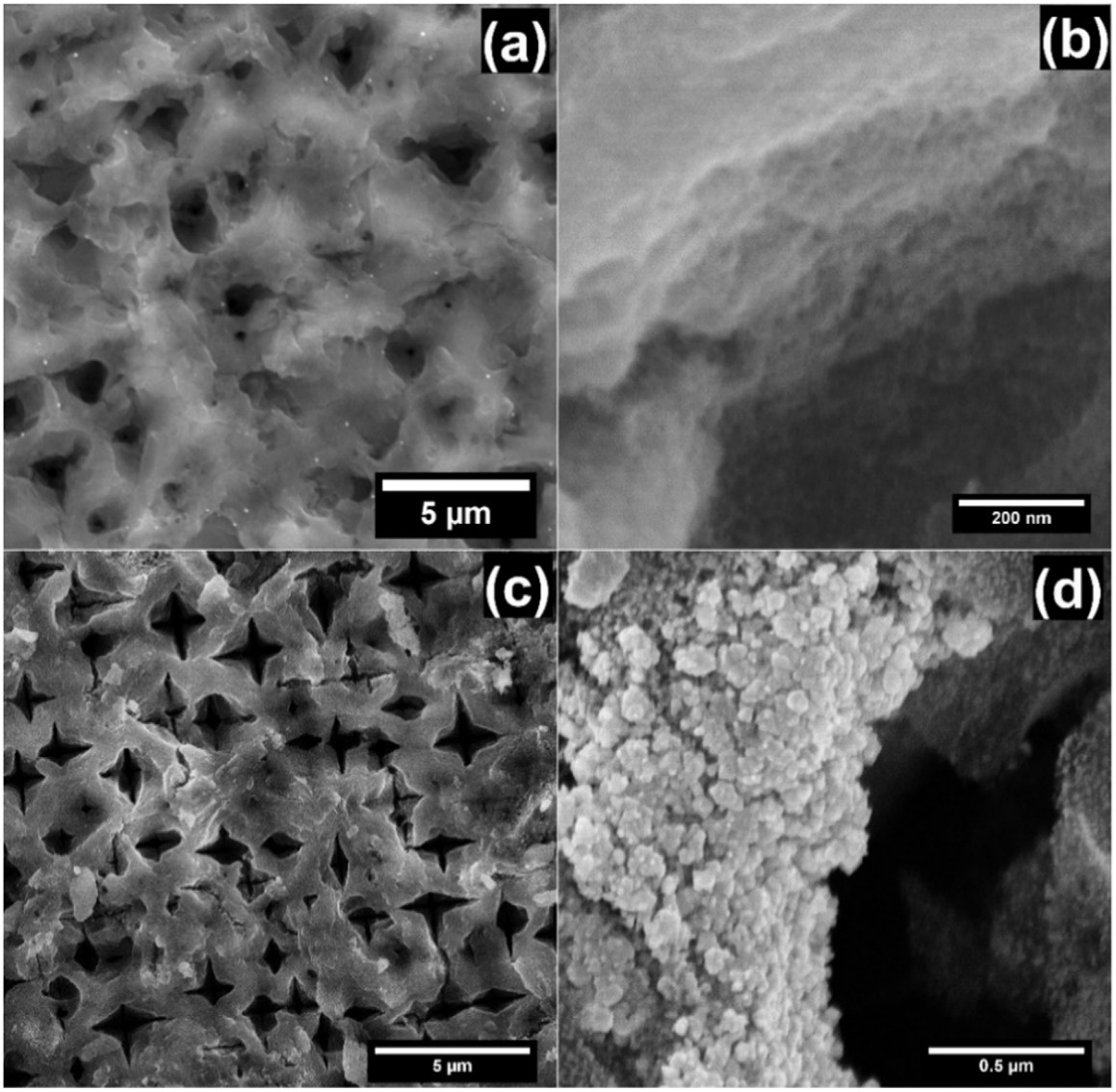

Fig. 2. Top-view SEM images of (a and b) PSi (111) structure; (c) PSi/Au$_{(Chem.^{20})}$ structure, (d) PSi/Au$_{(Chem.^{48})}$ structure.

Au^0 during chemical deposition (Fig. S2). The initial phase of chemical deposition of Au layer is based on electrostatic interaction between $[AuCl_4]^-$ ions and PSi surface. If additional electrical field is applied during electrochemical deposition than the process of the gold nucleation/deposition is significantly facilitated by electrochemical reduction of $[AuCl_4]^-$.

2.2. Optical properties of Si, PSi and PSi/Au structures

The main optical properties of Si, PSi and PSi/Au structures were studied by reflectance and photoluminescence (PL) spectroscopy. Fig. 3**a** shows the absolute reflectance of fabricated PSi and PSi/Au structures in the wavelength range of 400–850 nm. The optical reflectance of PSi decreases significantly comparing to polished Si surface. This result is consistent with that reported in previously published works [36,37]. The reflectance of PSi decreased by approximately 15% within the entire range of wavelengths due to the enhanced scattering and light absorption in the porous PSi. The total reflectance of the PSi/Au structures was lower or almost similar to that of PSi samples. While the reflectivity of PSi/Au structures increased especially in the range of 600–800 nm due to the gold layer formed on the PSi surface.

PL measurements were performed in order to assess the recombination ability of charge carriers at PSi/Au interface and to estimate the average size of Si nanocrystallites. In PSi/Au structure Au-based clusters are embedded within porous matrix of PSi therefore optical properties of PSi/Au are different from that of PSi due to additional scattering and/or SPR effect [24].

Fig. 3**b** shows PL spectra of PSi and PSi/Au structures registered at room temperature. The PL emission band centered at 675 ± 5 nm (1.84 eV) was observed for PSi and PSi/Au nanostructures (Fig. 3**b**). It is clearly seen, that PL spectra had more than one emission line. The deconvolution of PL spectrum into single peaks by Gaussian fitting, which was performed using Origin 8.5 software, divided the PL spectrum into four distinct peaks at 600, 675, 710 and 790 nm (Fig. S3). Red emission of PSi is related to the quantum confinement of electrons within Si nanocrystallites (nc) [38], therefore we suppose that a size distribution of Si nanocrystallites (nc-Si) in the PSi layer was significant. The average size of nc-Si was calculated by the following equation [39]:

$$E\,(eV) = E_g + \frac{h^2}{8d^2}\left[\frac{1}{m_e^*} + \frac{1}{m_h^*}\right], \tag{3}$$

where E(eV) = 1.84 eV, E_g = 1.12 eV, h – Planck's constant, $m_e^* = 0.19m_0$; $m_p^* = 0.16m_0$, $m_0 = 9.1 \times 10^{-31}$ kg. The calculated average

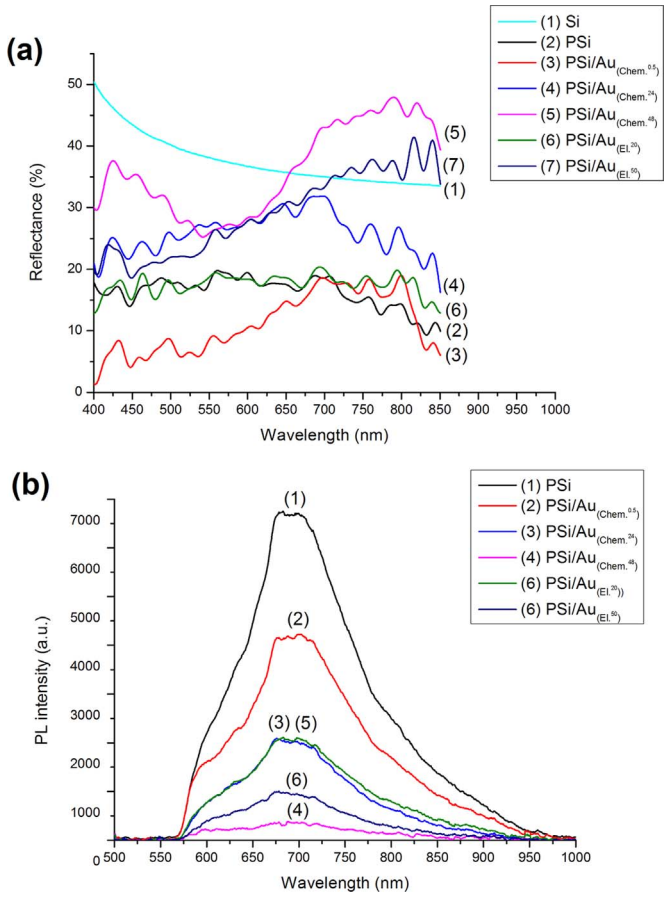

Fig. 3. (a) Reflectance spectra of Si, PSi and PSi/Au structures; (b) The PL spectra of PSi and PSi/Au structures.

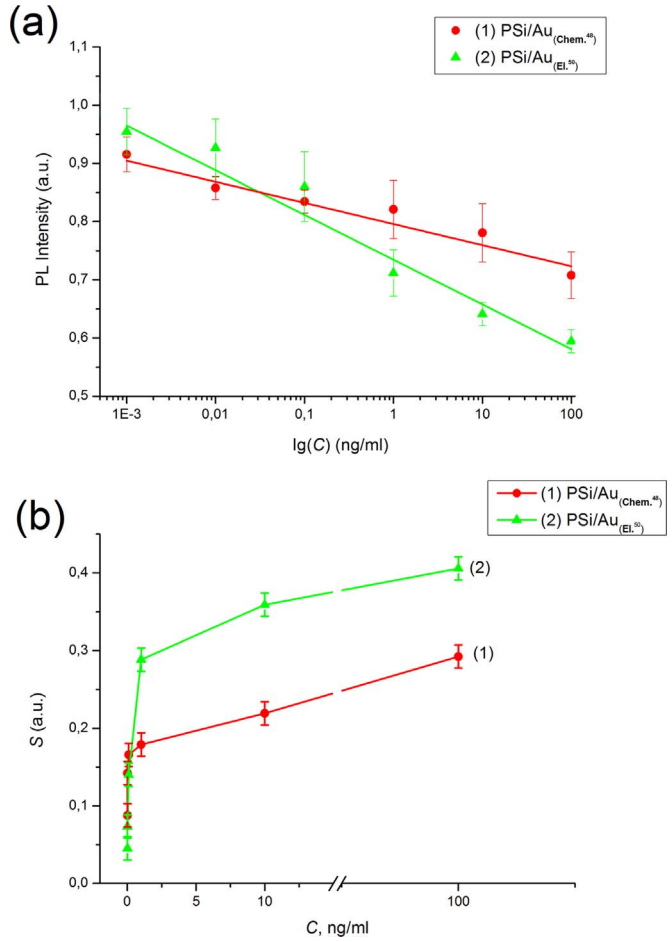

Fig. 4. (a) The dependence of PL intensity and (b) PL response of PSi/Au$_{(Chem.}^{48}$) /protein-A/anti-AFB1 and PSi/Au$_{(El.}^{50}$) /protein-A/anti-AFB1 structures on the logarithm of AFB1 concentration.

diameter of nc-Si was in the range of 2,5 nm corresponding to the values obtained by other authors [38,39].

The main peak of PL in PSi/Au structures remains at the same position 675 ± 5 nm (Fig. 3**b**). This picture illustrates that the PL intensity of PSi/Au structures decreases gradually depending on the thickness of deposited Au layer. Such decrease of PL according to de la Mora et al. [30] is based on three main factors: porosity, chemical surface modification, and plasmonic effects. All these factors are increasing the efficiency of PL quenching in PSi/Au nanocomposites compared to that of PSi and pristine Si substrate. Moreover it is well known that the oxidation of PSi leads to an increase of intensity and a blue shift of the PL peak [40]. In the observed PL spectra of PSi and PSi/Au structures both the PL peak position and the shape of spectra are very similar. Therefore, the oxidation and chemical modification of the surface can be excluded from possible reasons, which are inducing changes in PL spectra. Thus, the most probably that in PSi/Au structures the PL quenching is mostly effected by surface plasmon resonance of Au nanolayer [28,38]. The PL spectra of fabricated samples correlate with that reported in other researches where separated Au-nanoparticles were deposited on the PSi surface [41].

2.3. Determination of analytical characteristics of biosensors

During the evaluation of performance of biosensors based on PSi/Au$_{(Chem.}^{48}$)/protein-A/anti-AFB1 and PSi/Au$_{(El.}^{50}$)/protein-A/anti-AFB1 structures the PL signal permanently decreased with an increase of the analyte concentration (**SI,** Fig. S4). If 100 ng/ml of AFB1 were present in the cell, then the PL intensity decreased almost twice. There is a relationship between the PL intensity (I) and the logarithm of AFB1 concentrations, which is expressed as a linear calibration curves (Fig. 8): $I_{PSi/Au(Chem.48)} = 0.8 - 0.03\ \lg(C)$, and $I_{PSi/Au(El.50)} = 0.74 - 0.08\ \lg(C)$, respectively. The limit of detection (LOD) was determined using equation [42]:

$$LOD = 3.3\sigma/b, \quad (4)$$

where σ is the standard deviation in the presence of 'negative control' and b is the slope of the calibration curves (Fig. 4**a**). The calculated values of LOD were about 2.7 ± 0.11 pg/ml and 2.1 ± 0.11 pg/ml for immunosensors based on PSi/Au$_{(Chem.}^{48}$)/protein-A/anti-AFB1 and PSi/Au$_{(El.}^{50}$)/protein-A/anti-AFB1 structures, respectively. These estimated values of LOD were much better than that for previously reported electrochemical biosensors based on DNA-aptamers [43].

The immunosenor signal was normalized and the sensor response S was calculated according to this equation [44]:

$$S(C) = 1 - I_{eq}(C), \quad (5)$$

where I_{eq} is normalized signal value after the reaching of steady-state conditions at particular concentration (C) of AFB1.

The isotherms of interaction of AFB1 with PSi/Au$_{(Chem.}^{48}$)/protein-A/anti-AFB1 and PSi/Au$_{(El.}^{50}$)/protein-A/anti-AFB1 are plotted in the Fig. 4**b**. The isotherm of PSi/Au$_{(El.}^{50}$)/protein-A/anti-AFB1 sample has been saturated at high values of AFB1 concentrations. The isotherm of PSi/Au$_{(Chem.}^{48}$)/protein-A/anti-AFB1 sample tended to increase in all range of the measured AFB1 concentrations. We suppose that the interaction of AFB1 occurred according to the first order kinetics, which is the most probable in the case when dissolved materials are adsorbing on the surface of interphase and/or interacting with specific molecules (in this particular case such molecules are anti-AFB1) immobilized on this surface [45,46]:

$$\frac{dN}{dt} = k_a \cdot c \cdot (N_s - N) - k_d \cdot N, \quad (6)$$

where N, k_a, k_d, N_s and C are a number of adsorbed molecules, association constant, dissociation constant, number of adsorption sites and concentration, respectively.

After some time, when steady-state conditions are achieved, then the equation becomes valid:

$$\frac{dN}{dt} = 0. \quad (7)$$

The adsorption isotherm was analyzed using Langmuir (Eq. (8)) and Langmuir-Freundlich (Eq. (9)) equations:

$$\theta = \frac{B \cdot C}{K_D + C}, \quad (8)$$

$$\theta = \frac{B \cdot C^n}{K_D^n + C^n}, \quad (9)$$

where $\theta = \frac{N}{N_s}$ is surface coverage, $K_D = \frac{k_d}{k_a}$ – affinity dissociation constant and n – power coefficient, pointing to interaction between AFB1 and surface ($n < 1$). The analysis of the adsorption isotherms (**SI,** Fig. S5) better fitted when Langmuir-Freundlich equation was applied for the evaluation of the data. The calculated values of n and K_D are shown in the Table 1. According to here presented calculations, the power coefficient n for the interaction of AFB1 with PSi/Au$_{(El.}{}^{50})$/ protein-A/anti-AFB1 structures was determined to be around 0.5. Such low power coefficient could be related to limited diffusion of AFB1 within advanced surface structures of PSi/Au surface. The power coefficient for the interaction of AFB1 with PSi/Au$_{(Chem.}{}^{48})$/protein-A/anti-AFB1structure was equal 0.25. Such relatively low power coefficient most probably is related to more limited diffusion of AFB1 within advanced surface structures of PSi/Au$_{(Chem.}{}^{48})$ surface.

The interaction between AFB1 and anti-AFB1 and/or surface could be estimated by calculation of the Gibbs free energy (ΔG) using this equation [45,46]:

$$\Delta G = -R \cdot T \cdot \ln(K_{D0}), \quad (10)$$

where T and R are absolute temperature and universal gas constant, respectively. The value of K_{D0} was calculated as:

$$K_{D0} = \frac{K_D}{C}, \quad (11)$$

where C is an AFB1 concentration equal to 1 M.

According to the data, reported in Table 1, the toxin molecules showed more efficient adsorption onto the surface of PSi/Au$_{(Chem.}{}^{48})$/ protein-A/anti-AFB1 in comparison to PSi/Au$_{(El.}{}^{50})$/ protein-A/anti-AFB1 structures. The binding energy between AFB1 and to PSi/Au$_{(El.}{}^{50})$/ protein-A/anti-AFB1 surface was lower in comparison with that of between AFB1 and PSi/Au$_{(Chem.}{}^{48})$/protein-A/anti-AFB1.

Sensitivity of the biosensors was calculated as derivative of sensor signal (S) versus natural logarithm of the toxin concentration (C). According to Eq. (9), a dimensionless value of sensitivity was obtained after differentiation. The obtained results are shown in the Fig. 5. The sensitivity of PSi/Au$_{(El.}{}^{50})$-based samples showed maximum in the range of AFB1 concentrations 0.1–1 ng/ml. The sensitivity of PSi/Au$_{(Chem.48)}$-based samples showed minimum in the range of AFB1 concentrations 0.1–1 ng/ml and contentious increase at higher AFB1 concentrations. Analysis of the sensitivity was performed via estimation of full width of half maximum of the obtained curve. PSi/Au$_{(El.}{}^{50})$ /protein-A/anti-AFB1 structures showed the highest sensitivity to AFB1 in the range of 0.01–10 ng/ml. We have not performed testing of PSi/Au$_{(Chem.}{}^{48})$/protein-A/anti-AFB1 structures towards higher concentrations of AFB1. However, we can suppose that the lower sensitivity limit of PSi/Au$_{(Chem.}{}^{48})$/protein-A/anti-AFB1 structures starts in the range 1–5 ng/ml and the upper limit is over 100 ng/ml of AFB1 concentration. It is worth to mention that an average value of response time, which was calculated when 95% saturation of the analytical signal was observed, significantly decreased for PSi/Au$_{(Chem.}{}^{48})$/protein-A/anti-AFB1 (21 min) and PSi/Au$_{(El.}{}^{50})$/anti-AFB1 (18 min) structures. Thus, the deposition of Au layer within pores of PSi by electrochemical method resulted in the increase of sensitivity and the reduction of response time of PSi/Au$_{(El.}{}^{50})$/anti-AFB1 immunosensors to AFB1 molecules.

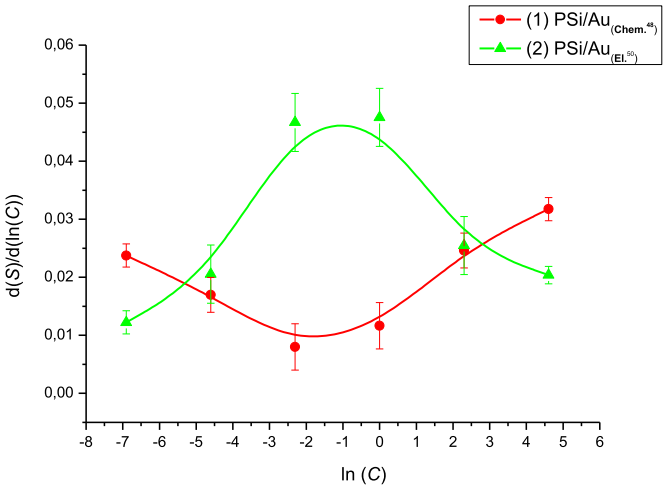

Fig. 5. Sensitivity of PSi/Au$_{(Chem.}{}^{48})$ /protein-A/anti-AFB1 and PSi/Au$_{(El.}{}^{50})$ /protein-A/anti-AFB1 structures towards different concentrations of AFB1.

Table 1
Registered characteristics of interaction between AFB1 and different structures.

Sample abbreviation	n	K_D, M	ΔG, J/mol
PSi/Au$_{(Chem.}{}^{48})$ /protein-A/ anti-AFB1	0.25 ± 0.04	$3.1 \cdot 10^{-10} \pm 0.22 \cdot 10^{-10}$	54601 ± 231
PSi/Au$_{(El.}{}^{50})$ /protein-A/ anti-AFB1	0.47 ± 0.07	$1.1 \cdot 10^{-10} \pm 0.15 \cdot 10^{-10}$	51532 ± 202

3. Conclusion

Novel PSi/Au structures were formed by chemical and electrochemical methods and they were applied in the design of PL-based immunosensors dedicated for the detection of AFB1. The morphology, chemical composition and optical properties of PSi and PSi/Au structures were evaluated. We observed clear decrease of the PL intensity PSi/Au/protein-A/anti-AFB1 structures with the increase of AFB1 concentration in samples. Such PL change has been used as analytical signal. Analytical characteristics of biosensors based on several different PSi/Au/protein-A/anti-AFB1 structures were evaluated and partially optimized. The calculated values of LOD were about 2.5 ± 0.5 pg/ml. Langmuir-Freundlich isotherms were plotted for the interaction of AFB1 with PSi/Au/protein-A/anti-AFB1 structures and some aspects of interaction mechanisms were determined. We have shown that formation of Au-based structures within pores of PSi by electrochemical method resulted in increase of sensitivity and decrease of response time of the immunosensors. Analytical performance of the Au/PSi immunosensor showed very good characteristic with maximal sensitivity range within 0.01–10 ng/ml. Comparing to the standard ELISA method, here proposed Au/PSi immunosensor has about 100 lower concentration range. PSi/Au/protein-A/anti-AFB1 structures show very promising properties suitable for PL-based immunosensors.

Table 2
Parameters applied in formation of different structures.

Sample abbreviation	Method	Deposition parameters
$PSi/Au_{(Chem.}^{0.5})$	Chemical deposition	30 min deposition
$PSi/Au_{(Chem.}^{20})$		20 h deposition
$PSi/Au_{(Chem.}^{48})$		48 h deposition
$PSi/Au_{(El.}^{20})$	Electro-chemical deposition	20 mV *vs* $Ag/AgCl_{(3\ M\ KCl)}$
$PSi/Au_{(El.}^{50})$		50 mV *vs* $Ag/AgCl_{(3\ M\ KCl)}$

4. Experimental section

4.1. Materials

The biological samples (antigens (Ag) and antibodies (Ab) of aflatoxine B1, protein A, bovine serum albumin (BSA)) and reagents (3-Triethoxysilylpropylamine (APTES), 11-Mercaptoundecanoic acid (11–MUA), N-Hydroxysuccinimide (NHS), N-(3-Dimethylaminopropyl)-N′-ethylcarbodiimide hydrochloride (EDC)), Si wafers and chemical materials were purchased from Sigma Aldrich.

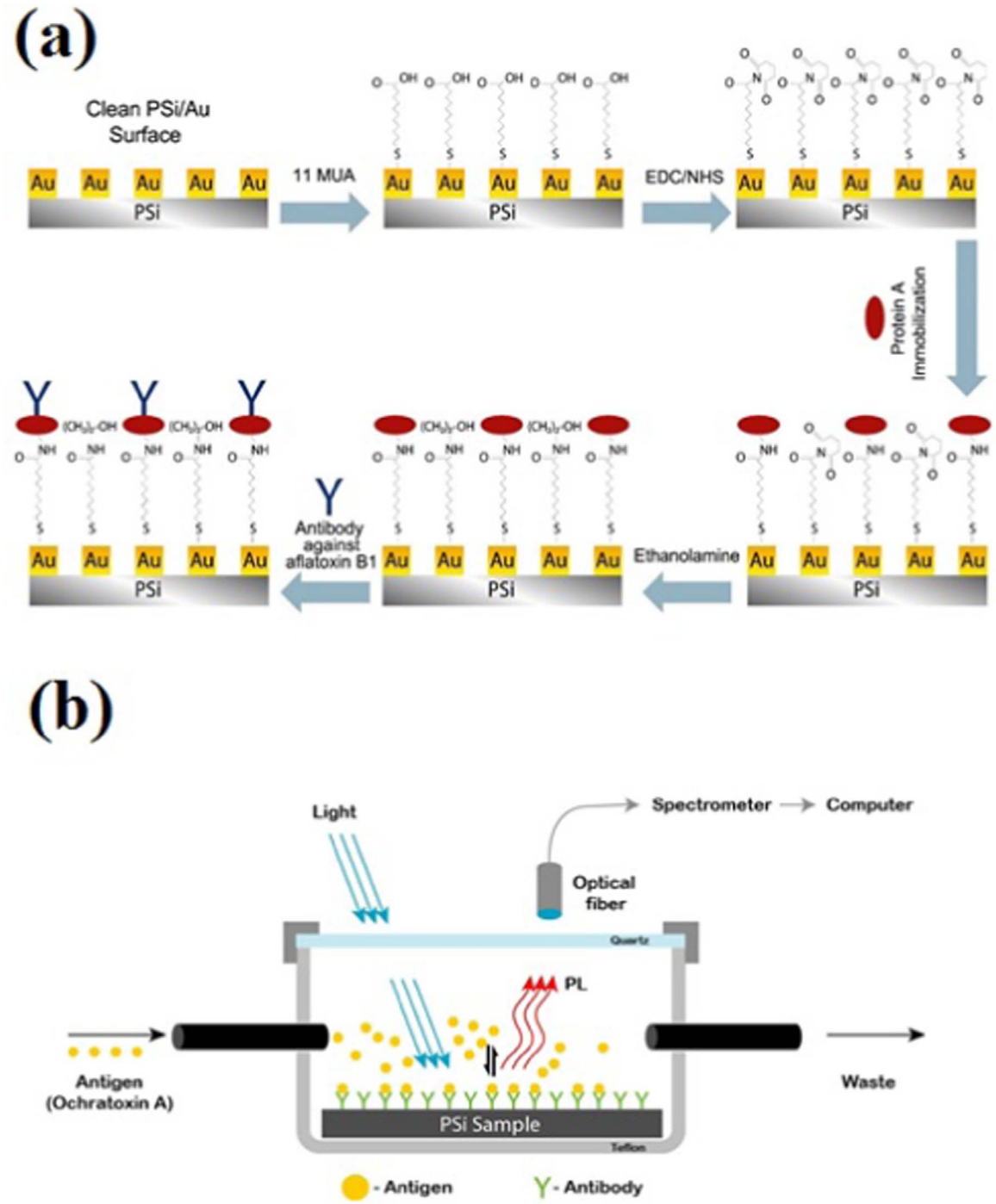

Fig. 6. (a) Sequence of procedures applied for the functionalization PSi/Au surface and immobilization of antibody against AFB1 (anti-AFB1); (b) The scheme of photoluminescence measurement based cell used for the evaluation of AFB1 and anti-AFB1 interaction kinetic.

4.2. Fabrication of PSi samples

The PSi samples were fabricated from highly doped p-type Si wafers (B-doped, ρ= 0.005 Ω cm) with (111) orientation utilizing metal assisted chemical etching (MACE) [34]. The silver particles were deposited on pre-cleaned Si samples by immersion in 0.2 M HF and 10^{-3} M $AgNO_3$ aqueous solutions. The duration of incubation in this solution was 60 s. Then, the samples were etched in aqueous solutions containing HF (40%), H_2O_2 (30%), and ultrapure H_2O at a ratio of 20/80/80H_2O_2/H_2O/HF for 60 min. After etching, the samples were incubated in HNO_3 solution to remove the silver particles for 10 min and then incubated in 5% HF solution to remove an SiO_2 layer from the Si wafer surface. During the final step, the samples were cleaned with deionized water and then dried in nitrogen flow. All mentioned procedures were performed at room temperature.

4.3. Fabrication of PSi/Au nanocomposites

PSi/Au nanocomposites were fabricated by chemical and electrochemical deposition and two different structures PSi/$Au_{(Chem.)}$ and PSi/$Au_{(El.)}$ were formed, respectively (Table 2).

Chemical deposition method included following steps: (i) solution A, which consisted of 10 ml of H_2O and 0,25 ml of 1% $HAuCl_4$, was heated up to 60 °C, and solution B, which consisted of 2 ml of 1% aqueous solution of trisodium citrate, 8 ml of H_2O, 15 μl of Tannin, was also heated up to 60 °C; then solutions A and B were mixed and heated up to 95 °C and after that PSi samples were incubated in this mixed solution for 0.5, 20, and 48 h, and three different structures (PSi/$Au_{(Chem.}{}^{0.5}$), (PSi/$Au_{(Chem.}{}^{20}$), PSi/$Au_{(Chem.}{}^{48}$)) were formed, respectively.

Electrochemical deposition of gold onto PSi samples was performed with a computerized potentiostat PGSTAT 30/Autolab from EcoChemie (Utrecht, The Netherlands) controlled by GPES 4.9 software in cyclic voltamperometry mode. The deposition was performed within 20 cycles with the potential −0.6 – 0 V *vs* Ag/$AgCl_{(3\ M\ KCl)}$. The scanning rate was 20 mV/s and 50 mV/s for two groups of samples, referred as PSi/$Au_{(El.}{}^{20}$) and PSi/$Au_{(El.}{}^{50}$), respectively. The electrolyte solution was prepared by the same method as for the chemical deposition. The electrodeposition of Au onto the PSi was carried out with a three-electrode cell. Platinum and Ag/$AgCl_{(3\ M\ KCl)}$ from Metrohm AG (Herisau, Switzerland) were used as an auxiliary and reference electrodes, respectively.

4.4. Characterization of PSi and PSi/Au nanocomposites

Fabricated PSi and PSi/Au structures were evaluated by a high resolution field emission scanning electron microscope (SEM) SU-70 (Hitachi, Japan) at accelerating voltage 30 keV. Structural properties of PSi and PSi/Au structures were characterized using Grazing Incidence X-ray Diffraction (GIXRD; BrukerD5000). Photoluminescence (PL), reflectance and PL biosensing tests were measured using high-resolution fiber optic spectrometer AvaSpec-ULS3648 from Avantes (Apeldoorn, Netherlands). The excitation of the PL was performed by solid state laser (405 nm, 1000 Hz, 10 mW).

4.5. Formation of self-assembled monolayers on PSi/Au structures and immobilization antibody against of aflatoxine B1

Clean PSi/Au samples were incubated in 1 mM solution of 11-Mercaptoundecanoic acid (11 MUA) in ethanol at room temperature for 18 h. Then carboxyl groups of 11-MUA were activated using a mixture containing 0.1 M of 1-Ethyl-3-(3-dimethylaminopropyl)carbodiimide (EDC) and 0.1 M of *N*-Hydroxysuccinimide (NHS) for 300 s. The activated PSi/Au was incubated in 10 mM sodium acetate buffer, pH 4.5, containing 5 μg/ml of protein A for 1000 s and in such way PSi/Au/protein-A structure was formed. The deactivation of not reacted activated carboxyl groups was performed by incubation in 1 M ethanolamine, pH 8.5, for 900 s. Then PSi/Au/protein-A samples were incubated in 6.7 μg/ml water-based solution of anti-AFB1 to form complex of anti-AFB1 with protein A, formed structure is indicated as PSi/Au/protein-A/anti-AFB1. The principle scheme of these modifications is shown in the Fig. 6**a.**

4.6. Immunosensor testing

Analytical characteristics of biosensors based on PSi/$Au_{(El.)}$/protein-A/anti-AFB1 and PSi/$Au_{(Chem.)}$/protein-A/anti-AFB1 structures were performed in a homemade experimental cell (Fig. 6**b**), which was made of Teflon. A cavity, which was dedicated for a sample, was isolated by optical quartz glass to provide an excitation by laser light and PL signal collection. The cell was equipped with inlet and outlet for biomolecules probes. Photoluminescence was excited with solid state laser (λ = 405 nm) and collected by optical fiber spectrometer using multimode optical fibers equipped with semispherical lenses. Before measurement, 200 microliters of buffer solution were injected into the cell. The PL signal of the sample at fixed wavelength (λ = 700 nm) was collected every 5 s. The sample was stored in buffer solution until the PL signal reached equilibrium. Then, 200 microliters of aliquots, which contained different concentrations of AFB1, were subsequently injected into the cell.

Acknowledgment

I.I. acknowledges the financial support from the National Science Centre (NCN) of Poland by the SONATA 11 project UMO-2016/21/D/ST3/00962, R.V. acknowledges the partial financial support BIOSENSORS-AGRICULT (Development of nanotechnology based biosensors for agriculture FP7-PEOPLE-2012-IRSES, contract nr. 318520).

Appendix A. Supplementary material

Supplementary data associated with this article can be found in the online version at doi:10.1016/j.talanta.2017.07.054.

References

[1] J. Yu, Current understanding on aflatoxin biosynthesis and future perspective in reducing aflatoxin contamination, Toxins (Basel) 4 (2012) 1024–1057. http://dx.doi.org/10.3390/toxins4111024.

[2] N. Das, J. Basu, C. Roychaudhuri, Graphene coated nanoporous silicon immunosensor for food toxin detection, Int. J. Adv. Eng. Sci. Appl. Math. 7 (2015) 204–209. http://dx.doi.org/10.1007/s12572-015-0144-z.

[3] M. McLean, M.F. Dutton, Cellular interactions and metabolism of aflatoxin: an update, Pharmacol. Ther. 65 (1995) 163–192. http://dx.doi.org/10.1016/0163-7258(94)00054-7.

[4] V. Dohnal, V. Dvořák, F. Malíř, V. Ostrý, T. Roubal, A comparison of ELISA and HPLC methods for determination of ochratoxin A in human blood serum in the Czech Republic, Food Chem. Toxicol. 62 (2013) 427–431. http://dx.doi.org/10.1016/j.fct.2013.09.010.

[5] A.C. Entwisle, A.C. Williams, P.J. Mann, P.T. Slack, J. Gilbert, P. Burdaspal, E. Eklund, J. Gardikis, B. Hald, M.P. Herry, K. Jørgensen, H. Kandler, R. Maas, M.L. Martins, S. Patel, M. Schuster, M. Solfrizzo, E. Strassmeir, R. Tiebach, T. Trogersen, Liquid chromatographic method with immunoaffinity column cleanup for determination of ochratoxin A in barley: collaborative study, J. AOAC Int. 83 (2000) 1377–1386.

[6] G.J. Soleas, J. Yan, D.M. Goldberg, Assay of ochratoxin A in wine and beer by high-pressure liquid chromatography photodiode array and gas chromatography mass selective detection, J. Agric. Food Chem. 49 (2001) 2733–2740. http://dx.doi.org/10.1021/jf0100651.

[7] I. Barna-Vetro, L. Solti, J. Teren, A. Gyongyosi, E. Szabo, A. Wolfling, Sensitive ELISA test for determination of ochratoxin A, J. Agric. Food Chem. 44 (1996) 4071–4074.

[8] M. Bougrini, A. Baraket, T. Jamshaid, A. El Aissari, J. Bausells, M. Zabala, N. El Bari, B. Bouchikhi, N. Jaffrezic-Renault, E. Abdelhamid, N. Zine, Development of a novel capacitance electrochemical biosensor based on silicon nitride for ochratoxin A detection, 2016. http://dx.doi.org/10.1016/j.snb.2016.03.166.

[9] C. Reiner-Rozman, C. Kotlowski, W. Knoll, Electronic biosensing with functionalized rGO FETs, Biosensors 6 (2016). http://dx.doi.org/10.3390/bios6020017.

[10] M. McKeague, R. Velu, K. Hill, V. Bardóczy, T. Mészáros, M. DeRosa, Selection and characterization of a novel DNA aptamer for label-free fluorescence biosensing of ochratoxin A, Toxins (Basel) 6 (2014) 2435–2452. http://dx.doi.org/10.3390/toxins6082435.

[11] Z. Lu, X. Chen, W. Hu, A fluorescence aptasensor based on semiconductor quantum dots and MoS2 nanosheets for ochratoxin A detection, Sens. Actuators B Chem. 246 (2017) 61–67. http://dx.doi.org/10.1016/j.snb.2017.02.062.
[12] A. Tereshchenko, V. Fedorenko, V. Smyntyna, I. Konup, A. Konup, M. Eriksson, R. Yakimova, A. Ramanavicius, S. Balme, M. Bechelany, ZnO films formed by atomic layer deposition as an optical biosensor platform for the detection of Grapevine virus A-type proteins, Biosens. Bioelectron. 92 (2017) 763–769. http://dx.doi.org/10.1016/j.bios.2016.09.071.
[13] A. Tereshchenko, M. Bechelany, R. Viter, V. Khranovskyy, V. Smyntyna, N. Starodub, R. Yakimova, Optical biosensors based on ZnO nanostructures: advantages and perspectives. A review, Sens. Actuators B Chem. 229 (2016) 664–677. http://dx.doi.org/10.1016/j.snb.2016.01.099.
[14] S. Dhanekar, S. Jain, Porous silicon biosensor: current status, Biosens. Bioelectron. 41 (2013) 54–64. http://dx.doi.org/10.1016/j.bios.2012.09.045.
[15] K. Urmann, J.-G. Walter, T. Scheper, E. Segal, Label-free optical biosensors based on aptamer-functionalized porous silicon scaffolds, Anal. Chem. 87 (2015) 1999–2006. http://dx.doi.org/10.1021/ac504487g.
[16] W.Y. Tong, M.J. Sweetman, E.R. Marzouk, C. Fraser, T. Kuchel, N.H. Voelcker, Towards a subcutaneous optical biosensor based on thermally hydrocarbonised porous silicon, Biomaterials 74 (2016) 217–230. http://dx.doi.org/10.1016/j.biomaterials.2015.09.045.
[17] C. RoyChaudhuri, A review on porous silicon based electrochemical biosensors: beyond surface area enhancement factor, Sens. Actuators B Chem. 210 (2015) 310–323. http://dx.doi.org/10.1016/j.snb.2014.12.089.
[18] J. Li, M.J. Sailor, Synthesis and characterization of a stable, label-free optical biosensor from TiO2-coated porous silicon, Biosens. Bioelectron. 55 (2014) 372–378. http://dx.doi.org/10.1016/j.bios.2013.12.016.
[19] I. Iatsunskyi, M. Jancelewicz, G. Nowaczyk, M. Kempiński, B. Peplińska, M. Jarek, K. Załęski, S. Jurga, V. Smyntyna, Atomic layer deposition TiO2 coated porous silicon surface: structural characterization and morphological features, Thin Solid Films 589 (2015) 303–308. http://dx.doi.org/10.1016/j.tsf.2015.05.056.
[20] J.W. Mares, J.S. Fain, S.M. Weiss, Variable conductivity of nanocomposite nickel oxide/porous silicon, Phys. Rev. B - Condens. Matter Mater. Phys. 88 (2013) 1–8. http://dx.doi.org/10.1103/PhysRevB.88.075307.
[21] G. Zhu, J.-T. Liu, Y. Wang, D. Zhang, Y. Guo, E. Tasciotti, Z. Hu, X. Liu, In situ reductive synthesis of structural supported gold nanorods in porous silicon particles for multifunctional nanovectors, ACS Appl. Mater. Interfaces 8 (2016) 11881–11891. http://dx.doi.org/10.1021/acsami.6b03008.
[22] M.L. Coluccio, S. De Vitis, G. Strumbo, P. Candeloro, G. Perozziello, E. Di Fabrizio, F. Gentile, Inclusion of gold nanoparticles in meso-porous silicon for the SERS analysis of cell adhesion on nano-structured surfaces, Microelectron. Eng. 158 (2016) 102–106. http://dx.doi.org/10.1016/j.mee.2016.03.045.
[23] Y. Zhao, L. Wang, J. Min, W. Shi, Effect of Au film and absorption groups on minority carrier life of porous silicon, Curr. Appl. Phys. 10 (2010) 871–873. http://dx.doi.org/10.1016/j.cap.2009.10.010.
[24] S.Sánchez De La Morena, G. Recio-Sánchez, V. Torres-Costa, R.J. Martín-Palma, Hybrid gold/porous silicon thin films for plasmonic solar cells, Scr. Mater. 74 (2014) 33–37. http://dx.doi.org/10.1016/j.scriptamat.2013.06.015.
[25] M. Sainato, L.M. Strambini, S. Rella, E. Mazzotta, G. Barillaro, Sub-parts per million NO2 chemi-transistor sensors based on composite porous silicon/gold nanostructures prepared by metal-assisted etching, ACS Appl. Mater. Interfaces 7 (2015) 7136–7145. http://dx.doi.org/10.1021/am5089633.
[26] H. Zhang, Z. Jia, X. Lv, Surface layer reflective index changes of Au nanoparticle functionalized porous silicon microcavity for DNA detection, Curr. Appl. Phys. 15 (2014) 870–876. http://dx.doi.org/10.1016/j.cap.2015.03.023.
[27] X. Li, J. Tan, J. Yu, J. Feng, A. Pan, S. Zheng, J. Wu, Use of a porous silicon-gold plasmonic nanostructure to enhance serum peptide signals in MALDI-TOF analysis, Anal. Chim. Acta 849 (2014) 27–35. http://dx.doi.org/10.1016/j.aca.2014.08.028.
[28] M. Thakur, M. Isaacson, S.L. Sinsabaugh, M.S. Wong, S.L. Biswal, Gold-coated porous silicon films as anodes for lithium ion batteries, J. Power Sources 205 (2012) 426–432. http://dx.doi.org/10.1016/j.jpowsour.2012.01.058.
[29] H. Dridi, A. Moadhen, L. Haji, Comparative SERS study carried out on unsilanized and silanized oxidized porous silicon surface coated by small gold nanoparticles, J. Porous Mater. 22 (2014) 239–245. http://dx.doi.org/10.1007/s10934-014-9890-8.
[30] M.B. De. La Mora, J. Bornacelli, R. Nava, R. Zanella, J.A. Reyes-Esqueda, Porous silicon photoluminescence modification by colloidal gold nanoparticles: plasmonic, surface and porosity roles, J. Lumin. 146 (2014) 247–255. http://dx.doi.org/10.1016/j.jlumin.2013.09.053.
[31] T.S.T. Amran, M.R. Hashim, N.K.A. Al-Obaidi, H. Yazid, R. Adnan, Optical absorption and photoluminescence studies of gold nanoparticles deposited on porous silicon, Nanoscale Res. Lett. 8 (2013) 35. http://dx.doi.org/10.1186/1556-276X-8-35.
[32] S. Sakamoto, L. Philippe, M. Bechelany, J. Michler, H. Asoh, S. Ono, Ordered hexagonal array of Au nanodots on Si substrate based on colloidal crystal templating, Nanotechnology 19 (2008) 405304. http://dx.doi.org/10.1088/0957-4484/19/40/405304.
[33] I. Iatsunskyi, E. Coy, R. Viter, G. Nowaczyk, M. Jancelewicz, I. Baleviciute, K. Załęski, S. Jurga, Study on structural, mechanical, and optical properties of Al2O3–TiO2 nanolaminates prepared by atomic layer deposition, J. Phys. Chem. C 119 (2015) 20591–20599. http://dx.doi.org/10.1021/acs.jpcc.5b06745.
[34] I. Iatsunskyi, M. Pavlenko, R. Viter, M. Jancelewicz, G. Nowaczyk, I. Baleviciute, K. Załęski, S. Jurga, A. Ramanavicius, V. Smyntyna, Tailoring the structural, optical, and photoluminescence properties of porous silicon/TiO2 nanostructures, J. Phys. Chem. C 119 (2015) 7164–7171. http://dx.doi.org/10.1021/acs.jpcc.5b01670.
[35] M.L. Chourou, K. Fukami, T. Sakka, Y.H. Ogata, Gold electrodeposition into porous silicon: comparison between meso- and macroporous silicon, Phys. Status Solidi Curr. Top. Solid State Phys. 8 (2011) 1783–1786. http://dx.doi.org/10.1002/pssc.201000094.
[36] M. Pavlenko, E.L. Coy, M. Jancelewicz, K. Zaleski, V. Smyntyna, S. Jurga, I. Iatsunskyi, Enhancement of optical and mechanical properties of Si nanopillars by ALD TiO2 coating, RSC Adv. 6 (2016) 97070–97076. http://dx.doi.org/10.1039/C6RA21742G.
[37] G. Rong, J.D. Ryckman, R.L. Mernaugh, S.M. Weiss, Label-free porous silicon membrane waveguide for DNA sensing, Appl. Phys. Lett. 93 (2008). http://dx.doi.org/10.1063/1.3005620.
[38] O. Bisi, S. Ossicini, L. Pavesi, Porous silicon: a quantum sponge structure for silicon based optoelectronics, Surf. Sci. Rep. 38 (2000) 1–126. http://dx.doi.org/10.1016/S0167-5729(99)00012-6.
[39] K.A. Salman, K. Omar, Z. Hassan, The effect of etching time of porous silicon on solar cell performance, Superlattices Microstruct. 50 (2011) 647–658. http://dx.doi.org/10.1016/j.spmi.2011.09.006.
[40] S.M. Prokes, Light emission in thermally oxidized porous silicon: evidence for oxide-related luminescence, Appl. Phys. Lett. 62 (1993) 3244–3246. http://dx.doi.org/10.1063/1.109087.
[41] B. Gelloz, H. Sano, R. Boukherroub, D.D.M. Wayner, D.J. Lockwood, N. Koshida, Stabilization of porous silicon electroluminescence by surface passivation with controlled covalent bonds, Appl. Phys. Lett. 83 (2003) 2342–2344. http://dx.doi.org/10.1063/1.1613812.
[42] Y. Liu, J. Yu, Y. Wang, Z. Liu, Z. Lu, An ultrasensitive aptasensor for detection of Ochratoxin A based on shielding effect-induced inhibition of fluorescence resonance energy transfer, Sens. Actuators B Chem. 222 (2016) 797–803. http://dx.doi.org/10.1016/j.snb.2015.09.007.
[43] K. Yugender Goud, G. Catanante, A. Hayat, S.M, K. Vengatajalabathy Gobi, J.L. Marty, Disposable and portable electrochemical aptasensor for label free detection of aflatoxin B1 in alcoholic beverages, Sens. Actuators B Chem. 235 (2016) 466–473. http://dx.doi.org/10.1016/j.snb.2016.05.112.
[44] R. Viter, V. Khranovskyy, N. Starodub, Y. Ogorodniichuk, S. Gevelyuk, Z. Gertnere, N. Poletaev, R. Yakimova, D. Erts, V. Smyntyna, A. Ubelis, Application of room temperature photoluminescence from ZnO nanorods for salmonella detection, IEEE Sens. J. 14 (2014) 2028–2034. http://dx.doi.org/10.1109/JSEN.2014.2309277.
[45] V. Ratautaite, D. Plausinaitis, I. Baleviciute, L. Mikoliunaite, A. Ramanaviciene, A. Ramanavicius, Characterization of caffeine-imprinted polypyrrole by a quartz crystal microbalance and electrochemical impedance spectroscopy, Sens. Actuators B Chem. 212 (2015) 63–71. http://dx.doi.org/10.1016/j.snb.2015.01.109.
[46] I. Baleviciute, V. Ratautaite, A. Ramanaviciene, Z. Balevicius, J. Broeders, D. Croux, M. McDonald, F. Vahidpour, R. Thoelen, W. De Ceuninck, K. Haenen, M. Nesladek, A. Reza, A. Ramanavicius, Evaluation of theophylline imprinted polypyrrole film, Synth. Met. 209 (2015) 206–211. http://dx.doi.org/10.1016/j.synthmet.2015.07.021.